




# Dry Wear Behavior of Cladded NiCoCrAlY Coating on Cast Iron at Elevated Temperatures

HAO LIU,<sup>1,2</sup> JIAN LIU ,<sup>1,5</sup> JINGBIN HAO,<sup>1</sup> HAIFENG YANG,<sup>1</sup>  
XIULI HE,<sup>3,4</sup> and GANG YU<sup>3,4</sup>

1.—School of Mechanical and Electrical Engineering, China University of Mining and Technology, Xuzhou, China. 2.—Jiangsu Key Laboratory of Mine Mechanical and Electrical Equipment, China University of Mining and Technology, Xuzhou, China. 3.—Key Laboratory of Mechanics in Advanced Manufacturing, Institute of Mechanics, Chinese Academy of Sciences, Beijing, China. 4.—School of Engineering Science, University of Chinese Academy of Sciences, Beijing, China. 5.—e-mail: 15257130777@163.com

To improve the service life of valve retainer in the engine exhaust system, the NiCoCrAlY alloy coating was fabricated on compacted graphite cast iron by laser cladding. Microstructure and high-temperature wear resistance of the coating were studied. The coating exhibits a refined dendritic structure. The  $M_{23}C_6$  nano-precipitates with rod-shape are embedded the  $\gamma$ (Fe, Ni) solid solution dendrites, and the  $M_7C_3$  nano-precipitates are distributed in the inter-dendrite region. The average nano-hardness of the coating and the substrate are measured as 4.08 GPa and 3.96 GPa, respectively. The wear morphologies and coefficient of friction variation reveal that the friction layer formed at 25°C and 600°C is a mechanical mixing layer and a composite layer, respectively. The coating possesses excellent wear resistance at 600°C due to the formation of a dense oxide film. The main component of the oxide film is identified as  $Fe_2O_3$ ,  $Fe_3O_4$ ,  $Al_2O_3$ ,  $CrO_2$ ,  $CrO_3$  and  $Cr_2O_3$ .

## INTRODUCTION

The valve retainer, an important part of the engine exhaust system, plays a critical role in sealing the valve and extending the service life of the engine.<sup>1</sup> However, the high-temperature exhaust from the engine combustion chamber and the high-frequency impact from the moving parts in the exhaust system provide an extremely harsh working environment, which leads to strict requirements for the toughness and high-temperature wear resistance of the valve retainer.<sup>2</sup> Cast iron with excellent wear resistance is a common material for the manufacture of valve retainers.<sup>3</sup> However, the brittle fracture characteristic of cast iron can seriously threaten their regular operation. In this regard, it is a practical solution to deposit a coating with preeminent high-temperature wear resistance and toughness on the valve retainer.

MCrAlY (M = Ni, Co or NiCo) alloys with excellent thermal stability, wear resistance, and mechanical properties have been analyzed by many researchers.<sup>4–6</sup> The Ni-based alloy coatings are

commonly used as transition layers of thermal barrier coatings due to their outstanding adhesion and high elasticity modulus.<sup>7</sup> The wear behavior of the NiCoCrAlY alloy fabricated by spark plasma sintering at different temperatures has been investigated.<sup>8</sup> The NiCoCrAlY alloy exhibits a smaller wear rate (about  $5.20 \times 10^{-5} \text{ mm}^3 \text{ N}^{-1} \text{ m}^{-1}$ ) and better wear resistance at high temperature (600°C), compared with at room temperature (25°C). Thus, it is expected that the NiCoCrAlY alloy with favorable high-temperature wear resistance can satisfy the working conditions of valve retainers.

Some advanced technologies, such as plasma spraying<sup>9,10</sup> and laser cladding,<sup>11,12</sup> have been used to deposit coatings. Compared with the thermal spraying process, the coating fabricated by laser cladding possesses a better bonding strength of metal powders, which is conducive to the improvement of wear resistance.<sup>13,14</sup> Moreover, laser cladding can achieve good metallurgical bonding between coating and valve retainer.<sup>15</sup> The dense NiCoCrAlY coating has been prepared by laser cladding on austenitic stainless steel (AISI 304).<sup>11</sup>

The wear rate of the NiCoCrAlY coating composed of  $\gamma$ -Ni phase and  $\beta$ -NiAl phase was calculated to be about  $9.90 \times 10^{-5} \text{ mm}^3 \text{ N}^{-1} \text{ m}^{-1}$  at  $500^\circ\text{C}$ , while that at  $24^\circ\text{C}$  is  $1.63 \times 10^{-4} \text{ mm}^3 \text{ N}^{-1} \text{ m}^{-1}$ , approximately. The NiCoCrAlY coating exhibits satisfactory wear resistance at high temperature. The dilution effect of laser cladding inevitably leads to the mixing and diffusion of elements between the coating and the substrate, which may significantly change the microstructure and the phase constitution of the coating.<sup>16</sup> There are few reports about Ni-based coatings on cast iron surfaces in the literature. It is considered that the high carbon content in cast iron can change the microstructure and further affect the performance of Ni-based coatings. Thus, it is necessary to study the microstructure and the high-temperature wear resistance of the coating deposited on the surface of cast iron by laser cladding.

The main purpose of this content is to provide a meaningful reference for the practical application of Ni-based coatings working in high temperature, abrasion, and other environments by analyzing the wear resistance of coatings deposited on the surface of cast iron at elevated temperatures. The microstructure and phase constitution are characterized in detail. Meanwhile, the wear mechanism and the composition of the wear products are investigated.

## MATERIALS AND METHODS

### Preparation of Coating

The NiCoCrAlY alloy coating was prepared by laser cladding. The compacted graphite cast iron (CGI, RuT300) was selected as the substrate. The cast iron was cut into cuboids with dimensions of  $120 \text{ mm} \times 60 \text{ mm} \times 30 \text{ mm}$  by a wire-EDM machine (DK7745), and the cut substrate was ground and polished to remove the oxide layer. The surface of the substrate was cleaned with alcohol and acetone. The raw material of Ni-based alloy powder (2.6 wt.% Co, 18.6 wt.% Cr, 3.4 wt.% Al, 0.42 wt.% Y and Ni in balance) was dried in an electric vacuum drying oven (DZF-6020) for 6 h. The laser cladding was implemented by a fiber laser system (YLS-400-CTTC-Y11) with the following parameters: laser power of 900 W, powder feed rate of  $4.3 \text{ g min}^{-1}$ , laser spot diameter of 2 mm, scanning velocity of  $10 \text{ mm s}^{-1}$ , and overlap rate of 50%. High-purity argon with a flow rate  $5 \text{ L min}^{-1}$  was selected as the shielding gas to prevent the oxidation of powders during the cladding process.

### Characterization of the Coating

The Ni-based alloy coating was processed into several specimens with a size of  $10 \text{ mm} \times 10 \text{ mm} \times 10 \text{ mm}$ . The surface of the specimens was ground with 500-, 1200-, 2000-, and 3000-grit SiC abrasive paper for metallographs, and then polished to a

roughness of  $0.2 \mu\text{m}$  using a metallographic polishing machine (MTP-200). The specimen was etched by aqua regia for the microstructure observation. The microstructure observation and component identification of coating were carried out using a scanning electron microscope (SEM; Quanta 250) equipped with an energy dispersive spectrometer (EDS). Transmission electron microscopy (TEM) with selected area electron diffraction (SAED) was used for more detailed microstructural characterization. A specimen with a diameter of 3 mm and a thickness of 10 nm prepared by twin-jet technology was used for the TEM observations. The phase composition was characterized by x-ray diffraction (XRD; D8 Advance; Bruker) using  $\text{CuK}\alpha$  radiation with a current of 30 mA and a voltage of 40 kV. The nano-hardness along the depth direction of the coating was measured using a nano-indenter (U9820A Nano Indenter G200). The three-dimensional morphologies of indentations on the substrate and coating were investigated by atomic force microscopy with a scanning frequency of 1 Hz. The high-temperature wear tests were executed on a ball-on-disk high-temperature wear tester (SIEMENS, HT-1000) with the following parameters: normal load of 4 N, frequency of 8.93 Hz, friction radius of 3 mm and duration time of 30 min. A commercial  $\text{Si}_3\text{N}_4$  ball was used as the counterpart. The wear tests were carried out at temperatures of  $25^\circ\text{C}$ ,  $200^\circ\text{C}$ ,  $400^\circ\text{C}$  and  $600^\circ\text{C}$ . The morphologies of the worn surfaces were observed by SEM.

## RESULTS AND DISCUSSION

### Phase Constitution and Microstructure

Figure 1 shows the XRD pattern of the Ni-based alloy coating prepared by laser cladding. The typical face-centered cubic (FCC) peaks, which are in good agreement with the standard diffraction patterns of the  $\gamma$ (Fe, Ni) phase, can be found in the XRD pattern of the coating. The lattice parameter corresponding

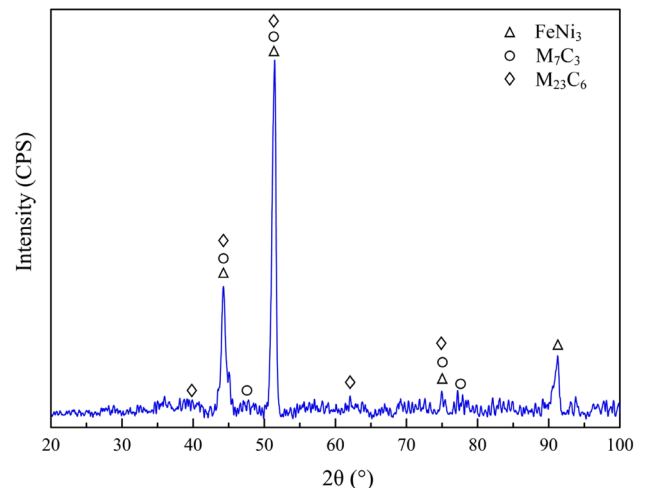


Fig. 1. XRD pattern of the laser-cladded Ni-based alloy coating.

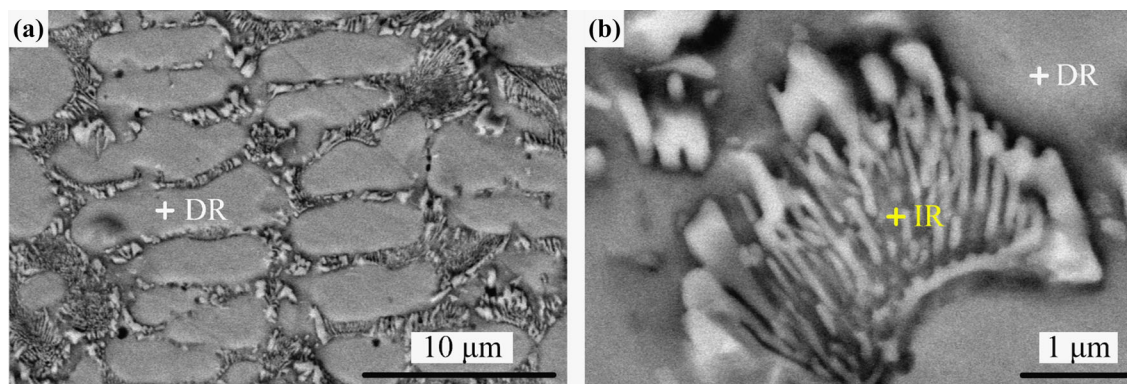


Fig. 2. SEM and TEM images of the Ni-based alloy coating: (a) SEM image of the coating; (b) magnified view of the IR.

**Table I. Microchemical composition of the investigated areas of the Ni-based coating (at.%)**

| Regions | Fe (at.%) | Ni (at.%) | Cr (at.%) | Si (at.%) | Al (at.%) | C     | Co   |
|---------|-----------|-----------|-----------|-----------|-----------|-------|------|
| DR      | 18.75     | 31.94     | 6.36      | 1.70      | 2.07      | 37.59 | 1.59 |
| IR      | 12.33     | 12.89     | 16.35     | 1.54      | 0.78      | 55.35 | 0.67 |

to the FCC phase has been calculated as approximately 0.354 nm. In addition, the diffraction peaks of the  $M_7C_3$  phase with a hexagonal structure and the  $M_{23}C_6$  phase with an FCC structure appear in the diffraction pattern of the Ni-based alloy coating.

The SEM images of the Ni-based alloy coating are displayed in Fig. 2. The typical dendritic morphologies can be observed in Fig. 2a. The average secondary dendritic arm spacing is calculated to be approximately  $3.07 \mu\text{m}$ . An enlarged view of the inter-dendritic region (IR) is shown in Fig. 2b, from which it can be seen that the IR region is mainly composed of the lamellar precipitates with the discontinuous distribution. The chemical compositions of the dendrite region (DR) and IR are listed in Table I, from which it can be seen that the contents of Fe and Ni elements in the DR are significantly higher than that in the IR. Combined with the XRD result (Fig. 1), it can be preliminarily confirmed that the DR contains the  $\gamma(\text{Fe, Ni})$  phase with an FCC lattice. Moreover, the IR shows the enrichment of Cr and C elements.

According to the XRD results, there should be three phases in the Ni-based coating, which is inconsistent with the microstructure of the Ni-based coating observed from the SEM images. Thus, the microstructure of the coating has been further characterized by TEM, as shown in Fig. 3a and b. Figure 3a shows the bright-field TEM image of the Ni-based alloy coating. The IR presents a discontinuous black precipitated phase, which is consistent with the SEM results. In addition, there are rod-like nano-precipitates embedded in the matrix (gray area). A magnified image (Fig. 3b) of the DR shows that the orientation of the nano-precipitates with

diameters ranging from about 32.69 nm to 155.03 nm and lengths ranging from about 135.19 nm to 714.18 nm is random. From the SAED analyses results (Fig. 3c), the matrix is characterized as an FCC phase with a lattice parameter of 0.355 nm, which corresponds to the  $\gamma(\text{Fe, Ni})$  phase in the XRD results. The SAED pattern of the black precipitated phase (Fig. 3d) in the IR displays a complex hexagonal structure. Combined with the EDS results, the IR can be identified as the  $M_7C_3$  phase ( $M = \text{Fe, Cr}$ ). For the nano-precipitates in the DR, these nano-precipitates are identified as an FCC phase with the space group of  $Fm\bar{3}m$  (Fig. 3e). Therefore, the nano-precipitated phase is proved to be a  $M_{23}C_6$  phase ( $M = \text{Fe, Cr}$ ).

According to the reports in the literature, most Ni-based alloys are composed of  $\gamma\text{-Ni}$  as the matrix and  $\beta\text{-NiAl}$  as the intermetallic phase.<sup>17,18</sup> However, we obtained a Ni-based coating with a completely different phase composition. This is mainly attributed to the dilution effect of the laser cladding. Under the heating of the laser beam with high energy density, the surface of the substrate melts locally, and the elements contained in the substrate diffuse along the direction from the bottom of the molten pool to the surface of the coating. The elements diffused into the coating, such as Fe and C, increase the mixing entropy and reduce the Gibbs free energy of the Ni-based alloy coating, which is conducive to the formation of the  $\gamma(\text{Fe, Ni})$  phase. The formation of the  $M_7C_3$  and  $M_{23}C_6$  phases can be explained by the mixing enthalpies between atomic pairs. The mixing enthalpies of the atomic pairs among different elements contained in the Ni-based coating are listed in Supplementary Table I. The

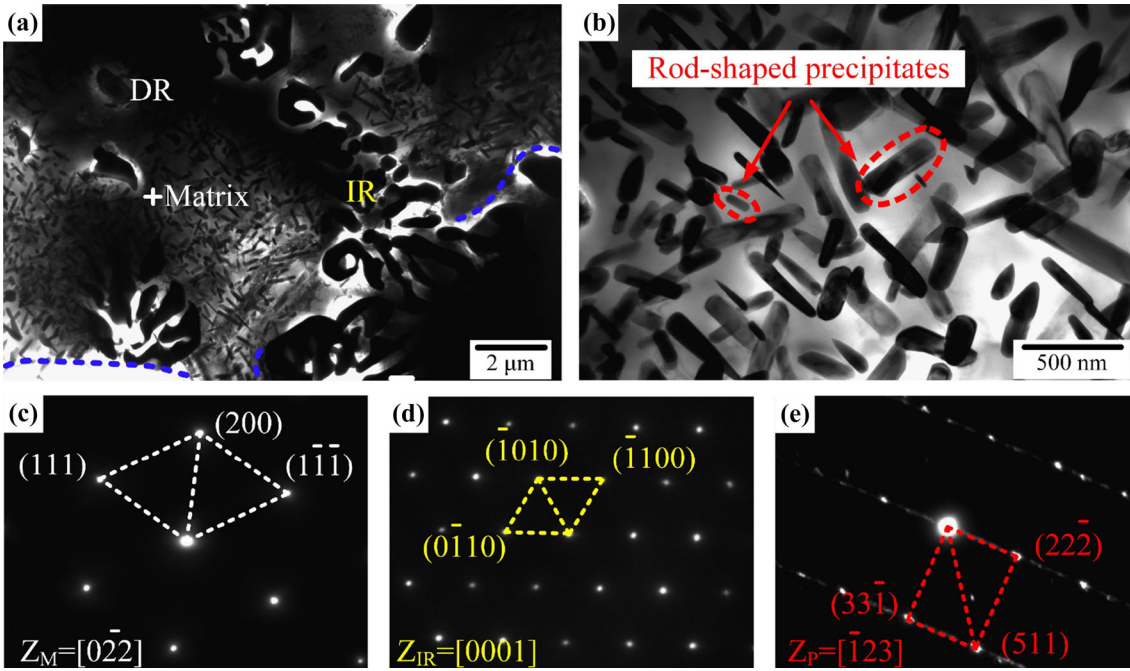


Fig. 3. TEM images of the coating: (a) bright-field TEM image of the coating; (b) magnified view of the DR; (c) SAED pattern of the matrix; (d) SAED pattern of the black precipitates; (e) SAED pattern of the nano-precipitates.

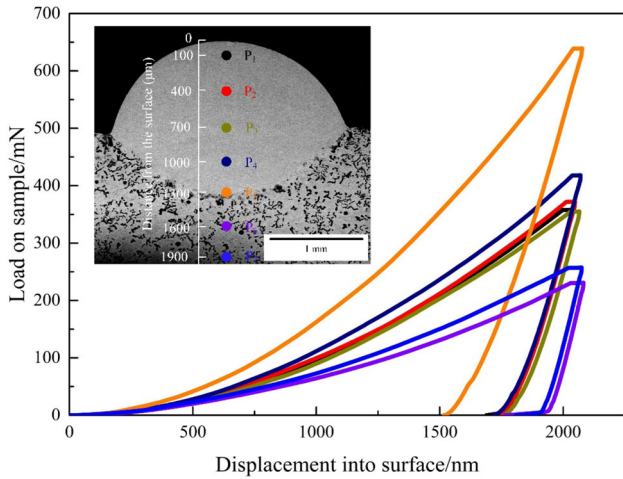


Fig. 4. Nanoindentation test results along the depth in the cross-section of the coating.

negative mixing enthalpies of Cr-C ( $-61 \text{ kJ mol}^{-1}$ ) and Fe-C ( $-50 \text{ kJ mol}^{-1}$ ) indicate the strong atomic affinity between the Fe, Cr and C atoms. Compared with other atoms, C atoms are more likely to combine with Fe and Cr atoms.

### Mechanical Properties

Figure 4 shows the results of the nanoindentation test along the depth direction in the cross-section of the coating. The exact location of the test points is presented in the upper left corner of Fig. 4. The load–depth curves reveal that the bonding zone

presents a larger load requirement when the maximum pressing depth is the same. The nano-hardness of the bonding zone is significantly higher than that of the coating and substrate, as shown in Supplementary Fig. 1. According to our previous work, the above phenomena can be explained by the martensitic transformation in the bonding zone.<sup>19</sup> The average nano-hardnesses of the coating, bonding zone and substrate are calculated to be about 4.08 GPa, 7.41 GPa and 3.96 GPa, respectively. It can be found that the average nano-hardness of the coating is higher than that of the CGI substrate. The three-dimensional morphologies of indentations on the substrate and coating are shown in Supplementary Fig. 2(a) and (c), respectively. There is a larger plastic deformation area on both sides of the indentation on the surface of the Ni-based coating. Also, the results of the height analysis (Supplementary Fig. 2(b) and (d)) present a higher proportion of the deformation area on the coating surface. The above results show that the Ni-based alloy coating has better plasticity than the substrate. The elastic modulus and stiffness of the coating are calculated to be about 190.92 GPa and  $1.53 \text{ N m}^{-1}$ , while those of the substrate are about 216.84 GPa and  $1.74 \text{ N m}^{-1}$ , respectively.

The improvement of the nano-hardness of the Ni-based coating can be attributed to the nano-precipitated phase. According to the Orowan's mechanisms,<sup>20,21</sup> the precipitated phases in the IR area and nano-precipitated phases in the DR can effectively hinder the slip of dislocations, leading to the formation of high-density dislocation pile-up groups,

as shown in Supplementary Fig. 3. The dislocation pile-up group around the  $M_7C_3$  precipitated phase in the IR area is demonstrated in Supplementary Fig. 3(a). Moreover, Supplementary Fig. 3(b) shows a high-density dislocation accumulation in the DR. The enlarged image of the DR area (Supplementary Fig. 3(c)) shows that the high-density dislocations mainly concentrate around the nano-precipitates. Also, the nano-precipitates, as impenetrable particles, promote encirclement of dislocations and formation of dislocation loops, as shown in Supplementary Fig. 3(d). Therefore, the nano-precipitated phase can play an effective role of second-phase strengthening, thus improving the hardness of the coating.

### Wear Behavior

SEM micrographs of wear scars of the Ni-based coating at elevated temperatures are shown in

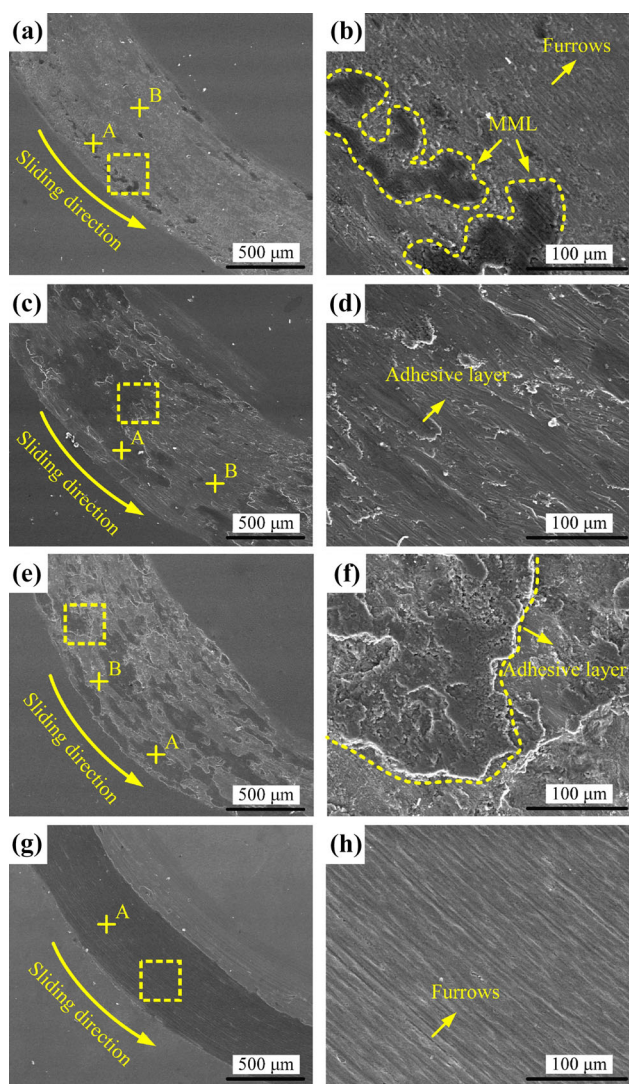


Fig. 5. SEM micrographs of wear scars of the Ni-based alloy coating at different temperatures: (a), (b) 25°C; (c), (d) 200°C; (e), (f) 400°C; (g), (h) 600°C.

Fig. 5. The worn surface of the Ni-based coating presents a relatively flat wear scar at 25°C, and only black friction layers (denoted as A) exist on both sides of the wear scar, as shown in Fig. 5a. The enlarged view of area A (Fig. 5b) shows that the distribution of the friction layer is discontinuous. Area A is considered to be a mechanical mixing layer (MML), which is formed by the extrusion and adhesion of debris.<sup>22</sup> In addition, dense furrows, the typical morphology characteristics of abrasive wear, can be seen in Fig. 5b. It can be concluded that the main wear mechanism of the Ni-based coating is abrasive wear at 25°C. Comparing the morphologies of worn surfaces at 200°C with that at 25°C, an obvious difference can be observed. The adhesive layer appears on the worn surface of coating at 200°C, as shown in Fig. 5c. It can be seen from the magnified view of the adhesive layer (Fig. 5d) that the deformation direction of the adhesive layer is parallel to the sliding direction, implying the occurrence of adhesive wear during wear at 200°C. The increase of temperature results in the softening of the surface of the Ni-based coating. Therefore, the surface material of the coating is easier to be torn and smeared under the action of external loading. The worn surface shows a thicker and rougher adhesive layer at 400°C (Fig. 5e and f). The further increase of temperature promotes the occurrence of adhesion wear and the deformation of the adhesion layer. However, it is worth noting that the wear morphology at 600°C shows a distinct difference compared with that at the other temperatures. From Fig. 5g, the Ni-based coating exhibits a smooth and complete wear scar. The approximate width of the wear scar at 600°C measures 550.4 μm, while the width of the wear scars at 25°C, 200°C and 400°C are about 808.5 μm, 944.5 μm and 1100.2 μm, respectively. Moreover, only regular and parallel furrows can be observed in the magnified image of the worn surface (Fig. 5h). All these results show that the Ni-based coating exhibits excellent wear resistance at 600°C.

The excellent wear resistance of the Ni-based coating is attributed to the formation of a composite layer (CL) on the worn surface at 600°C.<sup>23</sup> The material torn from the coating surface is extruded and sintered under the action of external loading at high temperature. At this point, the worn surface of the coating is rough, which can result in a relatively high coefficient of friction. With the continuation of the wear test, the extruded and cohesive debris are uniformly coated on the worn surface of the coating, indicating the formation of the CL.<sup>23</sup> The dense CL layer with high coverage formed at 600°C prevents direct contact between the  $Si_3N_4$  ball and the inner material of the coating, which effectively prevents further loss of the material. The smooth surface of the CL can significantly reduce the coefficient of friction. The above process can be proved by the real-time coefficient of friction curve of the wear process. As shown in Fig. 6, the downward trend

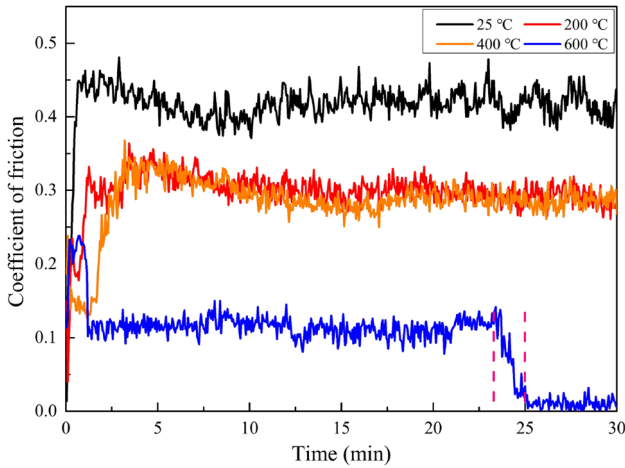


Fig. 6. Real-time coefficient of friction curves at elevated temperatures.

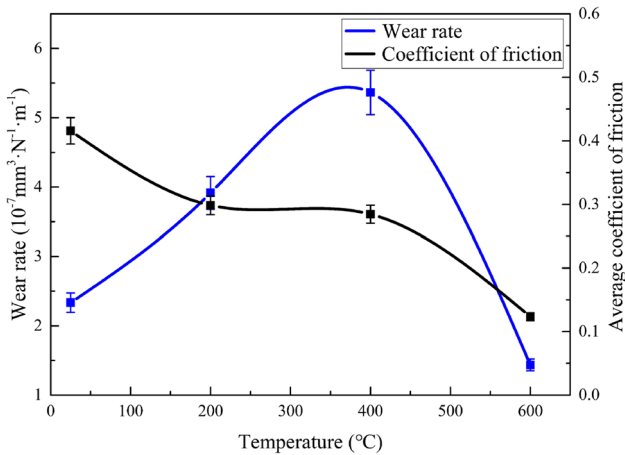


Fig. 7. Wear rate and the average coefficient of friction curves.

(from 23.35 min to 25.10 min) can be observed in the real-time friction coefficient curve of the coating tested at 600°C. It can be inferred that the complete formation time of the CL is about 25.10 min at 600°C. Figure 7 shows the average coefficient of the friction curve and the volume wear rate curve of the Ni-based coating at elevated temperatures, from which it is evident that temperature has a significant effect on the average coefficient of friction. With the increase of temperature, the average coefficient of friction gradually decreases. It is considered that the softening of the surface material promotes the deformation and smearing of the adhesive layer due to the increase of temperature, which can play an active role in lubrication. The volumetric wear rates of the coating at elevated temperatures are calculated to be  $2.23 \times 10^{-7} \text{ mm}^3 \text{ N}^{-1} \text{ m}^{-1}$ ,  $3.92 \times 10^{-7} \text{ mm}^3 \text{ N}^{-1} \text{ m}^{-1}$ ,  $5.37 \times 10^{-7} \text{ mm}^3 \text{ N}^{-1} \text{ m}^{-1}$  and  $1.44 \times 10^{-7} \text{ mm}^3 \text{ N}^{-1} \text{ m}^{-1}$ , respectively. The coating exhibits the minimum wear rate at 600°C, indicating that the coating has excellent wear resistance at high temperature.

The detailed microchemical compositions of different areas of the wear scars at elevated temperatures are listed in Supplementary Table II. The content of the O element in the MML is significantly higher than that in the naked area (denoted as B) at 25°C. The oxidation of the MML can be explained by the following. Firstly, the generation of friction heat promotes the oxidation and adhesion of deformed debris, and secondly, the heat released by the process of debris extrusion also promotes the occurrence of the oxidation reaction. It can also be seen from Supplementary Table II that the proportion of O atoms in the A area gradually increases with the increase of temperature. The CL area shows the highest concentration of the O element at 600°C. The friction layers (MML and CL) formed on the worn surface at different temperatures are oxidized during the wear process. Hereafter, all the friction layers are considered as the oxide layer. The coverage of the oxide layer formed on the worn surface at 25°C, 200°C, 400°C and 600°C is calculated to be 5.5%, 23.7%, 78.8% and 100%, respectively.

The XPS results of worn surfaces formed at 25°C and 600°C are displayed in Supplementary Fig. 4. The elements contained in the coating can be confirmed by the XPS survey spectrum (Supplementary Fig. 4(a)). The narrow spectrum of C shows a C1s peak at approximately 284.6 eV, indicating the accuracy of narrow scanning,<sup>24</sup> as shown in the illustration in the lower left corner of Supplementary Fig. 4(a). From Supplementary Fig. 4(b), it can be seen that the narrow spectrum of Co is almost unchanged at 25°C and 600°C, which indicates that there is no oxidation behavior of Co in the process of high-temperature wear. Different from the performance of Co, there are significant variations in the narrow spectrums of Ni2p, Fe2p, Cr2p and Al2p between 25°C and 600°C, as shown in Supplementary Fig. 4(c), (d), (e) and (f), respectively. The peaks of Ni(0), Fe(0), Cr(0) and Al(0), which exist in the narrow spectrum at 25°C, disappear at 600°C. Meanwhile, the Ni(oxide), Fe(oxide), Cr(oxide) and Al(oxide) peaks appear at 800°C, meaning that the main components are oxides of Ni, Fe, Cr and Al in the oxide layer.

The XPS high-resolution spectrums of Fe, Al, Ni and Cr at 600°C are shown in Supplementary Fig. 5. For Fe2p (Supplementary Fig. 5(a)), the peaks at 714.3 eV and 711.3 eV illustrate the existence of Fe<sub>2</sub>O<sub>3</sub>, while the peaks at 712.4 eV and 711.1 eV prove the presence of Fe<sub>3</sub>O<sub>4</sub>. The high-resolution spectrum of Al2p (Supplementary Fig. 5(b)) indicates the existence of Al<sub>2</sub>O<sub>3</sub> and a small amount of Al metal. The oxidation products of Ni and Cr during the wear process at 600°C can be observed in Supplementary Fig. 5(c) and (d). Ni element exists in the oxide layer as Ni<sub>2</sub>O<sub>3</sub> and NiO, while the oxides of Cr are mainly CrO<sub>2</sub>, CrO<sub>3</sub> and Cr<sub>2</sub>O<sub>3</sub>. As mentioned above, the main components of

the oxide layer are confirmed as  $\text{Fe}_2\text{O}_3$ ,  $\text{Fe}_3\text{O}_4$ ,  $\text{Al}_2\text{O}_3$ ,  $\text{CrO}_2$ ,  $\text{CrO}_3$  and  $\text{Cr}_2\text{O}_3$ .

### CONCLUSION

- (a) The NiCoCrAlY alloy coating cladded onto the surface of compacted graphite cast iron shows a dendritic structure. The DR region consists of a matrix of a  $\gamma(\text{Fe}, \text{Ni})$  solid solution phase and nano-precipitates of the  $\text{M}_{23}\text{C}_6$  intermetallic compound with rod-shape, and the IR region is composed of the  $\text{M}_7\text{C}_3$  phase.
- (b) The average nano-hardness of the coating and the substrate are measured at 4.08 GPa and 3.96 GPa, respectively. The improvement of the nano-hardness of the Ni-based alloy coating can be attributed to the nano-precipitated phase, which plays an effective role of second-phase strengthening.
- (c) With the increase of temperature, the wear mechanism changes from abrasive wear to adhesive wear and oxidation wear. The friction layer on the wear scar tested at  $25^\circ\text{C}$  is identified as a mechanical mixing layer, which is formed by the extrusion and adhesion of debris. However, the friction layer formed at  $600^\circ\text{C}$  is considered to be a composite layer, proved by the sudden drop in the friction coefficient curve.
- (d) The NiCoCrAlY alloy coating exhibits the best wear resistance at  $600^\circ\text{C}$ . The volumetric wear rates of the coating at elevated temperatures are calculated to be  $2.23 \times 10^{-7} \text{ mm}^3 \text{ N}^{-1} \text{ m}^{-1}$ ,  $3.92 \times 10^{-7} \text{ mm}^3 \text{ N}^{-1} \text{ m}^{-1}$ ,  $5.37 \times 10^{-7} \text{ mm}^3 \text{ N}^{-1} \text{ m}^{-1}$  and  $1.44 \times 10^{-7} \text{ mm}^3 \text{ N}^{-1} \text{ m}^{-1}$ , respectively.
- (e) The oxidation film formed on the worn surface at high temperature effectively improves the wear resistance of the coating. The main components of the oxide films are identified as  $\text{Fe}_2\text{O}_3$ ,  $\text{Fe}_3\text{O}_4$ ,  $\text{Al}_2\text{O}_3$ ,  $\text{CrO}_2$ ,  $\text{CrO}_3$  and  $\text{Cr}_2\text{O}_3$ .

### ACKNOWLEDGEMENTS

The authors acknowledge the Natural Science Foundation of Jiangsu Province (Grant No. BK20160258), the China Postdoctoral Science Foundation (Grant No. 2015M581881), and a Project Funded by Priority Academic Program Development of Jiangsu Higher Education Institutions (PAPD).

### ELECTRONIC SUPPLEMENTARY MATERIAL

The online version of this article (<https://doi.org/10.1007/s11837-019-03858-1>) contains supplementary material, which is available to authorized users.

### REFERENCES

1. C. Soffritti, M. Merlin, R. Vazquez, A. Fortini, and G.L. Garagnani, *Eng. Fail. Anal.* 92, 528–538 (2018).
2. P. Forsberg, P. Hollman, and S. Jacobso, *Wear* 271, 2477–2484 (2011).
3. A. Kalyon, *High Temp. Mater. Pr-Isr.* 34, 635–641 (2015).
4. M.W. Bai, B. Song, L. Reddy, and T. Hussain, *J. Therm. Spray Technol.* 28, 1–14 (2019).
5. Y. Zhang, B. Bates, J. Steward, and S. Dryepondt, *Oxid. Met.* 91, 95–112 (2019).
6. P.M. Zhang, R.L. Peng, X.H. Li, and S. Johansson, *Coatings* 8, 1–17 (2018).
7. U. Schulz, C. Leyens, K. Fritscher, M. Perter, B.-B. Saruhan, O. Lavigne, J.M. Dorvaux, M. Poulain, R. Mevrel, and M.L. Caliez, *Aerosp. Sci. Technol.* 7, 73–80 (2003).
8. S.L. Cao, S.F. Ren, J.S. Zhou, Y.J. Yu, L.Q. Wang, C. Guo, and B.B. Xin, *J. Alloys Compd.* 740, 790–800 (2018).
9. L.D. Zhao, M. Parco, and E. Lugscheider, *Surf. Coat. Technol.* 184, 298–306 (2004).
10. C. Tao, L. Wang, and X. Song, *Int. J. Min. Met. Mater.* 24, 222–228 (2017).
11. J. Pereira, J. Zambrano, M. Licausi, M. Tobar, and V. Amigo, *Wear* 330, 280–287 (2015).
12. H. Liu, J. Liu, P.J. Chen, and H.F. Yang, *Opt. Laser Technol.* 118, 140–150 (2019).
13. Y. Shi, C. Ni, J. Liu, and G.L. Huang, *Mater. Sci. Technol.* 34, 1239–1245 (2018).
14. K.M. Wang, D. Du, H. Liu, B.H. Chang, J. Ju, S.T. Sun, and H.G. Fu, *J. Alloys Compd.* 802, 373–384 (2019).
15. L. Jiang, W. Wu, Z.Q. Cao, D.W. Deng, and T.J. Li, *J. Therm. Spray Technol.* 25, 806–814 (2016).
16. Q. Lai, R. Abrahams, W.Y. Yan, C. Qiu, P. Mutton, A. Paradowska, X.Y. Fang, M. Soodi, and X.H. Wu, *Mater. Sci. Eng. A* 712, 548–563 (2018).
17. J.C. Pereira, J.C. Zambrano, E. Rayon, A. Yanez, and V. Amigo, *Surf. Coat. Technol.* 338, 22–31 (2018).
18. Y. Chen, X.F. Zhao, and P. Xiao, *Acta Mater.* 159, 150–162 (2018).
19. H. Liu, J.B. Hao, Z.T. Han, G. Yu, X.L. He, and H.F. Yang, *J. Mater. Process. Technol.* 232, 153–164 (2016).
20. L.J. Zhang, Z.K. Jiang, M.D. Zhang, J.T. Fan, D.J. Liu, P.F. Yu, G. Li, and R.P. Liu, *J. Alloys Compd.* 769, 27–36 (2018).
21. Y.F. Li, Y.M. Gao, B. Xiao, T. Min, Y. Yang, S.Q. Ma, and D.W. Yi, *J. Alloys Compd.* 509, 5242–5249 (2011).
22. B.M. Viswanatha, M.P. Kumar, S. Basavarajappa, and T.S. Kiran, *Ind. Lubr. Tribol.* 70, 818–827 (2018).
23. A. Pauschitz, M. Roy, and F. Franek, *Tribol. Int.* 41, 584–602 (2008).
24. G. Jin, Z.B. Cai, Y.J. Guan, X.F. Cui, Z. Liu, Y. Li, M.L. Dong, and D. Zhang, *Appl. Surf. Sci.* 445, 113–122 (2018).

**Publisher's Note** Springer Nature remains neutral with regard to jurisdictional claims in published maps and institutional affiliations.